

**RESEARCH ARTICLE**

10.1029/2017MS001225

**Key Points:**

- RCE simulations by the GFDL FV3 CRM exhibit remarkable sensitivity to the divergence damping
- Divergence damping, while acting to smooth out small-scale noise, modifies the strength and width of convective updraft velocity
- Changes in the updraft vertical velocity in the model have strong influence on the simulated climate, that is, relative humidity, convective organization, and cloud radiative forcing

**Correspondence to:**

U. M. Anber,  
uanber@bnl.gov

**Citation:**

Anber, U. M., Jeevanjee, N., Harris, L. M., & Held, I. M. (2018). Sensitivity of radiative-convective equilibrium to divergence damping in GFDL-FV3-based cloud-resolving model simulations. *Journal of Advances in Modeling Earth Systems*, 10, 1527–1536. <https://doi.org/10.1029/2017MS001225>

Received 1 NOV 2017

Accepted 1 MAY 2018

Accepted article online 5 MAY 2018

Published online 10 JUL 2018

# Sensitivity of Radiative-Convective Equilibrium to Divergence Damping in GFDL-FV3-Based Cloud-Resolving Model Simulations

Usama M. Anber<sup>1</sup> , Nadir Jeevanjee<sup>2</sup> , Lucas M. Harris<sup>3</sup> , and Isaac M. Held<sup>3</sup> 

<sup>1</sup>Environmental and Climate Sciences Department, Brookhaven National Laboratory, Upton, NY, <sup>2</sup>Program in Atmospheric and Oceanic Sciences, Princeton University, Princeton, NJ, <sup>3</sup>Geophysical Fluid Dynamics Laboratory, NOAA, Princeton, NJ

**Abstract** Using a nonhydrostatic model based on a version of Geophysical Fluid Dynamics Laboratory's FV3 dynamical core at a cloud-resolving resolution in radiative-convective equilibrium (RCE) configuration, the sensitivity of the mean RCE climate to the magnitude and scale-selectivity of the divergence damping is explored. Divergence damping is used to reduce small-scale noise in more realistic configurations of this model. This sensitivity is tied to the strength (and width) of the convective updrafts, which decreases (increases) with increased damping and acts to organize the convection, dramatically drying out the troposphere and increasing the outgoing longwave radiation. Increased damping also results in a much-broadened precipitation probability distribution and larger extreme values, as well as reduction in cloud fraction, which correspondingly decreases the magnitude of shortwave and longwave cloud radiative effects. Solutions exhibit a monotonic dependence on the strength of the damping and asymptotically converge to the inviscid limit. While the potential dependence of RCE simulations on resolution and microphysical assumptions are generally appreciated, these results highlight the potential significance of the choice of subgrid numerical diffusion in the dynamical core.

## 1. Introduction

Nonhydrostatic models at cloud-resolving resolutions in nonrotating radiative-convective equilibrium (RCE) have received much attention in recent years (e.g., Robe & Emanuel, 2001; Tao et al., 1999; Tompkins & Craig, 1999). They continue to provide valuable insights into the complex interaction between the physics of moist convection, boundary layer, clouds and precipitation, radiative transfer, the underlying surface, and the dynamical core. Resolving moist convection in these models has built a degree of confidence in understanding and interpreting problems pertaining to the maintenance of the mean tropical relative humidity profile and cloud feedbacks (e.g., Kuang & Hartmann, 2007; Romps, 2011).

However, the implications of the set of approximations associated with the discretization of the equations governing the resolved flow (referred to as the dynamical core) have been almost taken for granted in these studies, and little attention has been given to the effect of these aspects of the model on the RCE simulations, other than exploration of the sensitivity to horizontal resolution (e.g., Muller & Held, 2012), and in the thesis of Zhou (2016). One aspect of the model of potential importance is the manner in which the cascades of energy, enstrophy, and moisture variance to smaller scales are controlled. All models contain explicit or implicit controls on the generation of small-scale variance through these cascades. If this small-scale variance is not controlled, the accumulation of variance near the grid scale leads to unrealistic spectral shapes (e.g., Jablonowski & Williamson, 2011; Williamson, 2008a, 2008b). In some models, this small-scale dissipation is explicit, while in others, the cascade may be handled within the design of the numerical advection scheme (e.g., Durran, 1999). In the Geophysical Fluid Dynamics Laboratory (GFDL) Finite-Volume Cubed-Sphere Dynamical Core (FV3; Lin, 2004; Putman & Lin, 2007), the enstrophy cascade and the cascade of tracer variance can be controlled implicitly by the model's finite-volume advection and associated monotonicity constraints, but the accumulation of variance in the divergent component of the horizontal flow often requires separate control. In global models with this dynamical core, at lower resolution than the simulations discussed here, the flow can become noisy without this added divergence damping.

Second-order horizontal diffusion as a means to control grid-scale noise can directly affect the flow at resolved scales due to lack of scale selectivity (Jablonowski & Williamson, 2011). Therefore, higher-order diffusion ( $\nabla^4$  and higher) is generally chosen to improve the scale selectivity and has been the standard in

©2018. The Authors.

This is an open access article under the terms of the Creative Commons Attribution-NonCommercial-NoDerivs License, which permits use and distribution in any medium, provided the original work is properly cited, the use is non-commercial and no modifications or adaptations are made.

global hydrostatic models for decades. In many models, especially many spectral models (e.g., Taylor & Fournier, 2010), this higher order diffusion is applied to the total horizontal flow, that is, both the vorticity and divergence, and the detailed form of this dissipation can be of significance for the simulation (i.e., Williamson, 2008a, 2008b). In the global models based on hydrostatic versions of FV3 (Donner et al., 2011; Zhao et al., 2012, 2018a, 2018b), in which the enstrophy and tracer cascades are implicitly controlled by the advection scheme, a second-order diffusion designed to damp only the divergence of the horizontal flow is used in GFDL's Atmospheric Model 3 (AM3; Donner et al., 2011) while fourth-order diffusion is used in HiRAM (Zhao et al., 2012) and AM4.0 (Zhao et al., 2018a, 2018b).

In a study with a global model of most direct relevance to the present paper, Zhao et al. (2012), using HiRAM, found a nonintuitive monotonic increase in tropical storm frequency with the increase of the strength of fourth-order divergence damping. Outside of the tropics and on large scales within the tropics, the climate is insensitive to the strength of this damping. On cloud-resolving scales, the sensitivity to the numerical scheme and small-scale damping could be very different, however. For example, Holloway et al. (2013), using a large limited domain of the Met Office Unified Model version 7.1, showed that high-resolution simulation of Madden-Julian Oscillation (MJO) with explicit convection and 3-D Smagorinsky subgrid scheme captures the active phase of MJO to a very good extent, while simulation at the same resolution but with 2-D Smagorinsky scheme for horizontal mixing and boundary layer scheme for vertical subgrid mixing loses the large-scale MJO organization. Some discussion of the sensitivity of convective organization in cloud-resolving models (CRMs) in the RCE configuration to numerical and subgrid schemes is found in Zhou (2016, Ch. 5).

In this paper, we discuss the impact of the choice of grid-scale explicit diffusion in the FV3 dynamical core, namely, the order of the damping of the divergent component of the horizontal wind and its coefficient, on deep moist convection in radiative-convection equilibrium leading to changes in clouds, precipitation, and radiative fluxes. It is worth mentioning that both divergent and vortical components of the flow near the grid scale experience damping in FV3; divergence damping is made explicit, while damping of the vortical modes is implicit through monotonicity constraints (Lin, 2004; Putman & Lin, 2007). The sensitivity to numerical damping parameters raises concerns about the robustness of RCE climates simulated by CRMs.

This manuscript is organized as follows: in section 2, we describe the model and the experimental design. In section 3, we discuss how different aspects of convection, clouds and precipitation, and radiative fluxes are affected by the divergence damping. We summarize in section 4.

## 2. Model and Experimental Design

Our model is based on the nonhydrostatic version of the FV3 described in Lin (2004) and Putman and Lin (2007), re-configured to use a doubly periodic domain rather than the cubed-sphere grid used in global simulations. Unless otherwise stated, the model column physics is taken from the GFDL-AM4.0 (Zhao et al., 2018a, 2018b). The domain is  $64 \times 64 \times 51$  grid cells in  $(x, y, z)$ , with horizontal resolution of 500 m, and varying vertical resolution from a few tens of meters in the lower levels to hundreds of meters in the upper levels with the lowest model level located at 996.7 hPa. At this high resolution, we disable the convective parameterizations (both shallow and deep) used in the global model. Our choice of the small domain size is motivated by the desire to minimize the effect of convective self-aggregation, a behavior in which convection clusters into a relatively small fraction of the domain leaving the rest of the domain dry (e.g., Bretherton et al., 2005; Held et al., 1993; Muller & Held, 2012).

The model applies an implicit subgrid Rayleigh damping to the total wind field above 50 hPa with a time scale of one day, converting the lost kinetic energy to heat. The model also has a sponge layer at the top 2 levels to prevent unphysical wave reflection off the top boundary. Coriolis parameter  $f$  is set to zero. We use the GFDL Mellor-Yamada-2.5 prognostic TKE subgrid scheme (Mellor & Yamada 1982; Nakanishi & Niino, 2006) with local vertical mixing in the boundary layer to parameterize vertical diffusion of surface turbulent fluxes. Cloud liquid and ice water are prognostic variables, and cloud fraction is computed from a simple diagnostic scheme assuming a subgrid-scale distribution of total water (Klein et al., 2005; Tompkins, 2002). Surface turbulent fluxes and radiation are fully interactive. Radiative forcing is configured using an equatorial annual-mean solar zenith angle to give solar irradiance of  $418.7 \text{ W/m}^2$ , and there is no seasonal or diurnal cycle. Ozone and aerosol profiles are constant and prescribed equatorial mean. All experiments are conducted with a fixed sea surface temperature of  $28 \text{ }^\circ\text{C}$  to approximate the averaged tropical surface temperature.

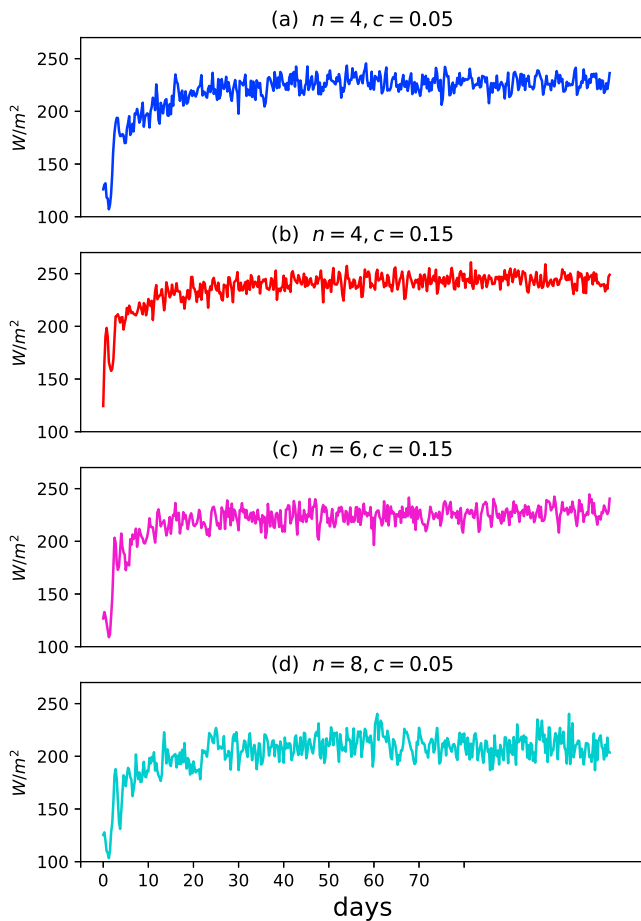


**Figure 1.** Time evolution of domain averaged OLR from 6-hr output for selected cases of divergence damping.

All experiments are run for more than 120 days, and analyses are made over the last 15 days of the simulations. Statistical equilibrium is reached roughly after 60 days as in Figure 1, which shows the domain averaged outgoing longwave radiation (OLR) for four selected cases of divergence damping: ( $n = 4, c = 0.15$ ), ( $n = 4, c = 0.05$ ), ( $n = 6, c = 0.15$ ), and ( $n = 8, c = 0.05$ ).

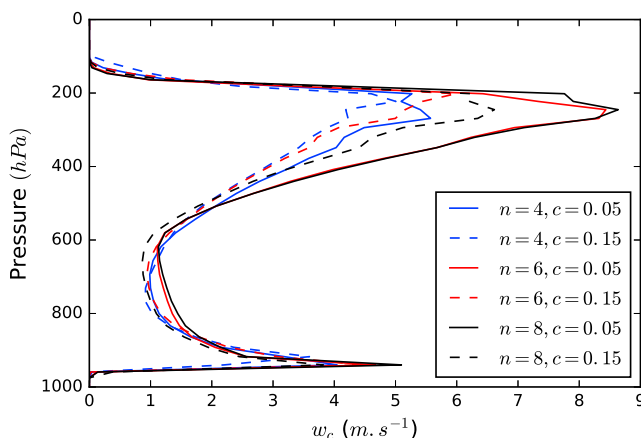


**Figure 2.** Mean convective updraft vertical velocity  $w_c$  averaged over convective cores (where liquid and ice condensate  $\geq 0.005$  kg/kg and  $w > 0$  m/s).

Divergence damping in FV3 is applied to the horizontal winds (Zhao et al., 2012; Lin & Harris, 2016, eq. (3) and (4)):

$$\mathbf{v}^{n+1} = \mathbf{v}^n + \dots + (-1)^N v_D \frac{\delta_x(\nabla^{2N} D)}{\Delta x} \quad (1)$$

where  $\mathbf{v} = (u, v)$ ,  $x = (x, y)$ ,  $N$  is a positive integer, and  $D$  is the divergence operator computed in its general form along a Lagrangian surface as

$$D = \frac{1}{A} [\delta_x(u\Delta y \sin\alpha) + \delta_y(v\Delta x \sin\alpha)]$$

where  $\delta_x$  is a centered-difference operator;  $\Delta x$  and  $\Delta y$  are the grid length in the  $x$  and  $y$  directions;  $\alpha$  is the angle between axes, for our flat domain here  $\alpha = \pi/2$ ; and  $A$  is the grid cell area. The damping parameter is given as

$$v_D = (c\Delta A_{min})^{N+1}$$

where  $N$  is 1 for the fourth order damping, 2 for the sixth order damping, etc.,  $\Delta A_{min}$  is the global minimum grid-cell area, and  $c$  is the non-dimensional damping coefficient. We will refer to the order of damping as  $n$ . For each  $n$ , we set  $c = 0.05$  and  $c = 0.15$ . This is similar to the range chosen in Zhao et al. (2012). The values of  $n = 4, c = 0.16$  are used in the AM4.0 version of the model (Zhao et al., 2018a, 2018b). However, in our simulations, for  $c > 0.15$ , the model becomes numerically unstable, which limits our choice of the strength of the damping coefficients designating weak and strong damping for  $c = 0.05$  and  $c = 0.15$ , respectively. We thus vary the order of the damping; that is,  $N = 1, 2, 3$  which give  $n =$  fourth-, sixth-, and eighth-order damping, respectively, in order to increase the parameter space in this study. It is important to note that divergence damping here is the only explicit subgrid numerical diffusion scheme we employ in the simulations.

### 3. Results

#### 3.1. Convective Mass Flux of Updrafts and Cold Pools

Damping the divergent component of the horizontal wind field leads to changes in the strength of vertical velocities through continuity, and therefore, the vertical distribution of heat and moisture in the atmospheric column. These convective mass fluxes of updrafts are key quantities for statistical description of convection. Convective mass fluxes, defined as  $\rho w_c / N_x, y$ , where  $\rho$  is the air density,  $N_x, y$  is the number of grid points, and  $w_c$  is the convective updraft vertical velocities averaged over convective cores, are depicted in Figure 2. Here convective cores are defined as grid points where cloud condensates (liquid + ice)  $\geq 0.005$  g/kg and  $w > 0$  m/s.

As shown in Figure 2, updrafts peak at 950 and 250 hPa, representing shallow and deep convection, respectively, with stronger peak at upper levels. As expected, simulation with strongest divergence damping ( $n = 4, c = 0.15$ ) exhibits the weakest updraft at all levels, though the lower peak

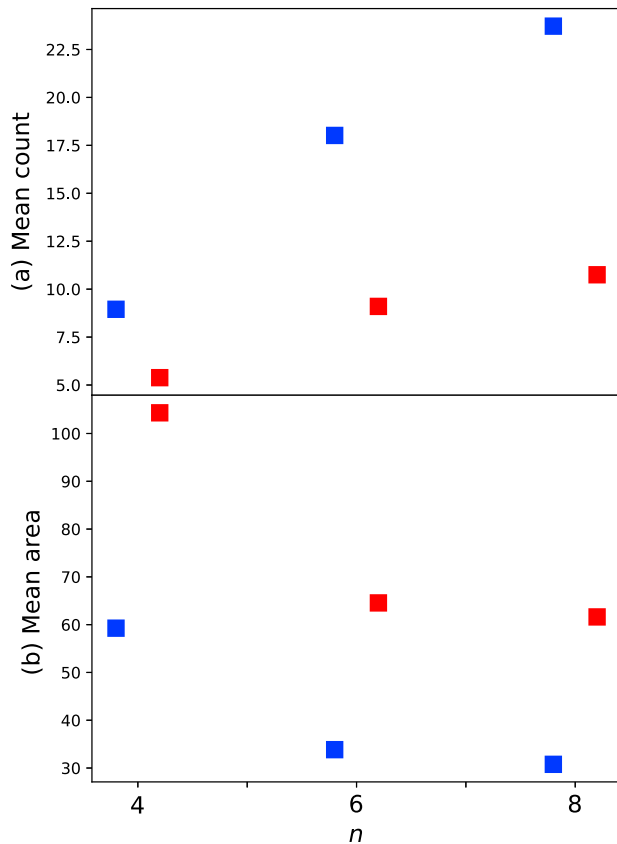


**Figure 3.** (a) Mean frequency of occurrence of convective updraft; (b) mean area (number of grid points) of individual convective updrafts in area units, from 6-hr output over the last 15 days of simulations. The blue and red squares for coefficient  $c = 0.05$  and  $c = 0.15$  for a given damping order  $n$ , respectively.

is attained at a slightly higher level than other damping magnitudes. The strongest updrafts are reached at the least damped divergence ( $n = 8$ ,  $c = 0.05$ ). Simulations with the sixth order and the same coefficient also show similar upper peak with a small reduction in the lower peak.

Updrafts show a monotonic behavior with respect to the damping coefficients at a given order  $n$ ; larger coefficient  $c = 0.15$  results in weaker updraft at the same order (comparison of dashed to solid lines of the same color). Monotonicity with respect to the order of damping for a given coefficient is also present (comparison among dashed or solid lines). The choice of cloud condensate threshold is somewhat arbitrary, and different thresholds produce different updraft magnitudes though the vertical structure and monotonicity remain the same.

Changes in the strength of convective updrafts as a response to damping are associated with the size they occupy; the stronger the damping, the weaker and the wider the updraft. Figure 3 shows the mean value of the probability distribution of the number (Figure 3a) and area (Figure 3b) of convective updrafts as a function of divergence damping from a 6-hourly output over the last 15 days of the simulations. Since, at equilibrium, the mean convective mass flux is constrained by energy balance; that is, convective heating is balanced by radiative cooling; the larger the area of convective updrafts, the less frequent they are in the domain (Figure 3b). Thus, updrafts that are less numerous and less well distributed in the horizontal are expected to be less effective at homogenous convective moistening, yet still effective at subsidence drying, leading to an overall reduction in relative humidity and stronger cold pools, which are driven by rain reevaporation and thus strongly tied to convective mass flux.

Cold pools are characterized by near surface negative buoyancy  $B = g$

$$\left(\theta_v - \theta'_v\right) / \theta'_v, \text{ where } \theta_v \text{ is the virtual potential temperature: } \theta_v = \theta(1 + 0.608q_v - q_l) \text{ where } q_v \text{ and } q_l \text{ are the mass mixing ratio for water vapor and liquid water, respectively; } g \text{ is the gravity acceleration; and over-}$$

bar denotes horizontal mean. Figure 4 shows snapshots of buoyancy at the lowest model level (in  $s^{-2}$ ) for the four selected cases as in Figure 1. It is clear that strong damping ( $n = 4$ ,  $c = 0.15$ ) results in more intense cold pools spreading over much wider areas than in weaker damping. Intensity of cold pools is quantified by a probability density function of negative buoyancy of magnitudes less than  $-0.005 \text{ m/s}^2$  (Tompkins, 2001), and shown in Figure 5. The outflow induced by the spread of cold pools mechanically lifts moist air at the edge of cold pools to trigger new convective cells (Jeevanjee & Romps, 2015; Rotunno et al., 1988); however, lower relative humidity in strong damping case inhibits further development of deep convection. In a weaker damping scenario (when relative humidity is higher as we will see in the next section), enhanced moisture and less cold near-surface temperature at the edges of cold pools result in more unstable environment favoring trigger of new convection, that is, thermodynamically induced convection (e.g., Feng et al., 2015; Torri et al., 2015), which also appears to impact convective organization as discussed in the next section.

### 3.2. Column Relative Humidity, Cloud Fraction, and Precipitation

Relative humidity is determined by a balance between convective moistening and subsidence drying (e.g., Romps, 2014). Figure 6a shows domain mean relative humidity for different damping parameters. Strongest damping ( $n = 4$ ,  $c = 0.15$ ) exhibits the driest column. Other damping cases of  $n = 4$ ,  $c = 0.05$  and  $n = 6$ ,  $c = 0.15$  have very similar structure with less dryness at 700 hPa, about 100 hPa higher than the driest case. The least damped case ( $n = 8$ ,  $c = 0.05$  and  $n = 6$ ,  $c = 0.05$ ) shows the least drying signal, with driest altitude at about 615 hPa, and 90% relative humidity in the upper troposphere above 500 hPa.

Overall, this picture is consistent with the convective mass flux of updraft in Figure 2 and the impact on mass flux and relative humidity ultimately links to the amount of cloud condensates deposited by the updrafts,

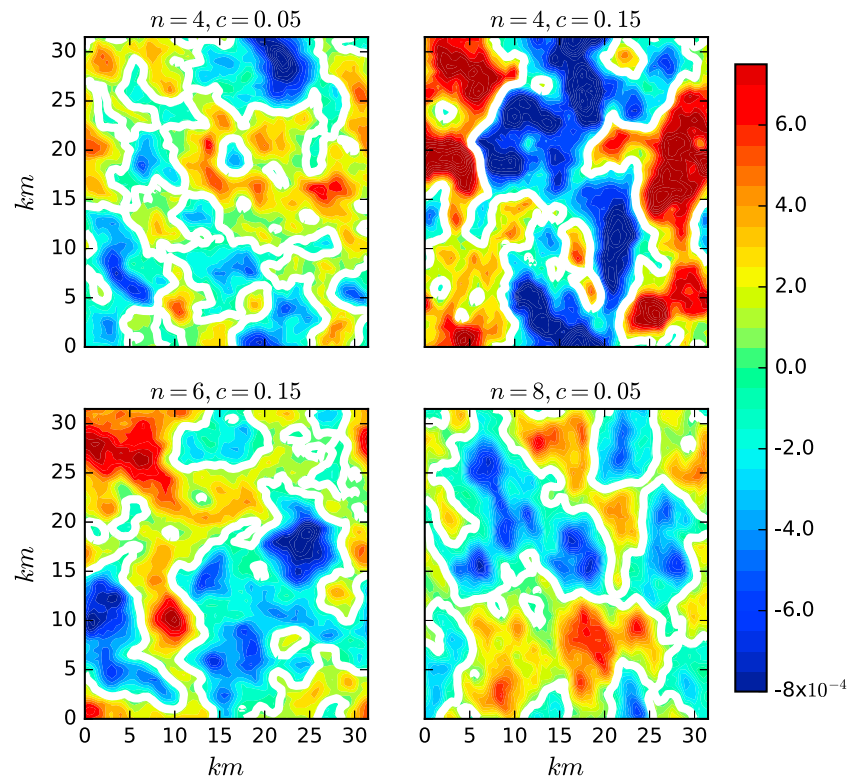


**Figure 4.** Near-surface mean buoyancy  $B$  ( $\text{m/s}^2$ ), illustrating cold pools (negative buoyancy) in blue shading. The white contours denote zero buoyancy.

quantitatively measured by cloud fraction which is shown in Figure 6b. Cloud fraction peaks at 950 and 200 hPa indicating shallow and deep convection, respectively. The effect of divergence damping on shallow clouds is rather small. However, deep convective clouds show significant differences. High cloud fractions exhibit a monotonic dependence on divergence damping parameters. The case of strongest damping ( $n = 4, c = 0.15$ ) shows the least amount of cloud fraction in the upper levels from 500 to 200 hPa consistent with the drying signal in relative humidity. Cases with higher orders of damping and smaller coefficients have more cloud fraction in the upper, particularly  $n = 8, c = 0.05$ , in which cloud fraction is a maximum.

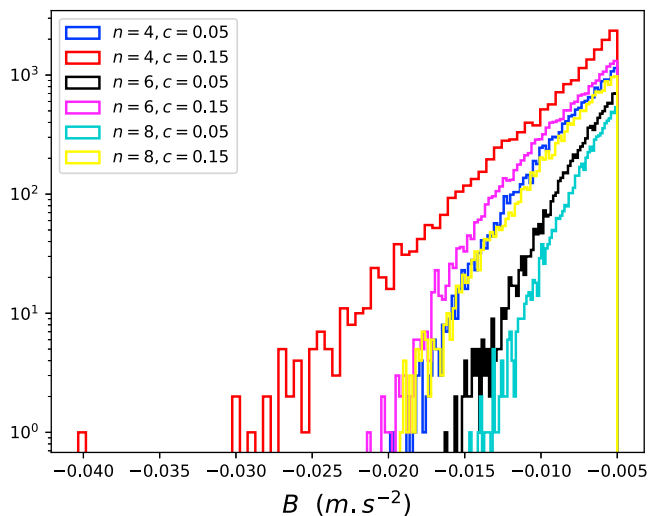


**Figure 5.** PDF of negative buoyancy ( $B$ ) at the first model level less than  $-0.005 \text{ m/s}^2$  threshold as an indicator for the strength of cold pools, calculated for all grid points from 6-hr output in the last 15 days of the simulations.

The degree of convection organization differs vastly with the divergence damping parameters as in Figure 7, which shows random snapshots of the spatial pattern of the OLR for four selected cases as in Figure 4. When damping is set to maximum (both order and magnitude), dry patches increase in intensity and extend over wider area. As damping weakens, convection tends to spread over larger areas, with less intense dryness. With the absence of wind shear in our simulations, this pattern is in alignment with that of the cold pools; the intensity and area of cold pools correlate well to the intensity and area of dry patches in the OLR field. Convective organization appears to be tied to the area of convective updraft in the domain as in Figure 8, which depicts this “linear” relationship with liquid water path and OLR fields (Figures 8a and 8b, respectively). The larger the area maintained by the updraft, the less liquid water path in the domain and the more OLR to space.

Given this dependence of relative humidity and cloud fraction on divergence damping parameters, we draw our attention to precipitation

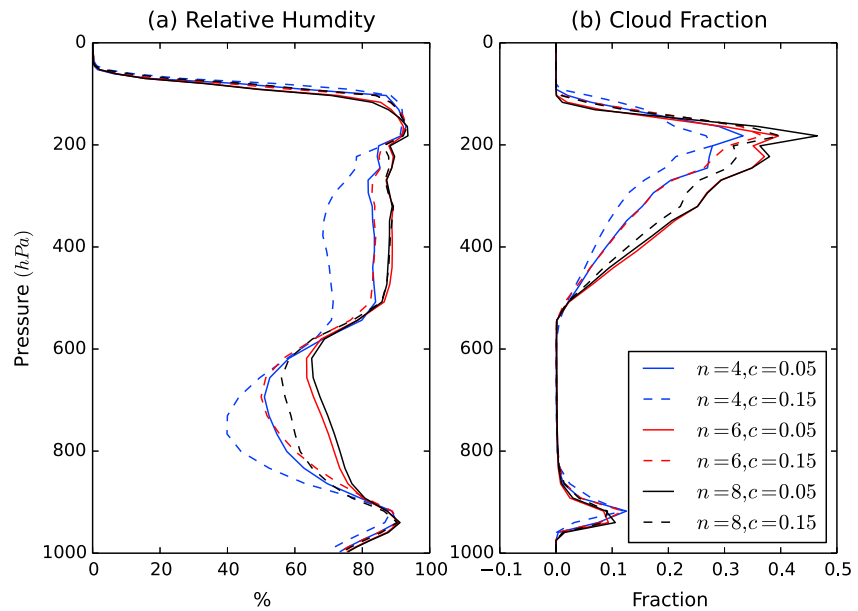


**Figure 6.** Domain mean (a) vertical profile of column relative humidity and (b) cloud fraction.

statistics. Figure 9 shows time-averaged frequency distribution of fraction of the time the tropical precipitation is in 0.5 mm/day bins ranging from 0 to 35 mm/day, calculated from 6-hr averages for all grid points. Variations in the divergence damping have a pronounced impact on extreme precipitation. Strong damping ( $n = 4, c = 0.15$ ) leads to a sharp increase in the likelihood of extreme precipitation events, while simulations with weaker damping, particularly ( $n = 8, c = 0.05$ ), have smaller chances of heavy

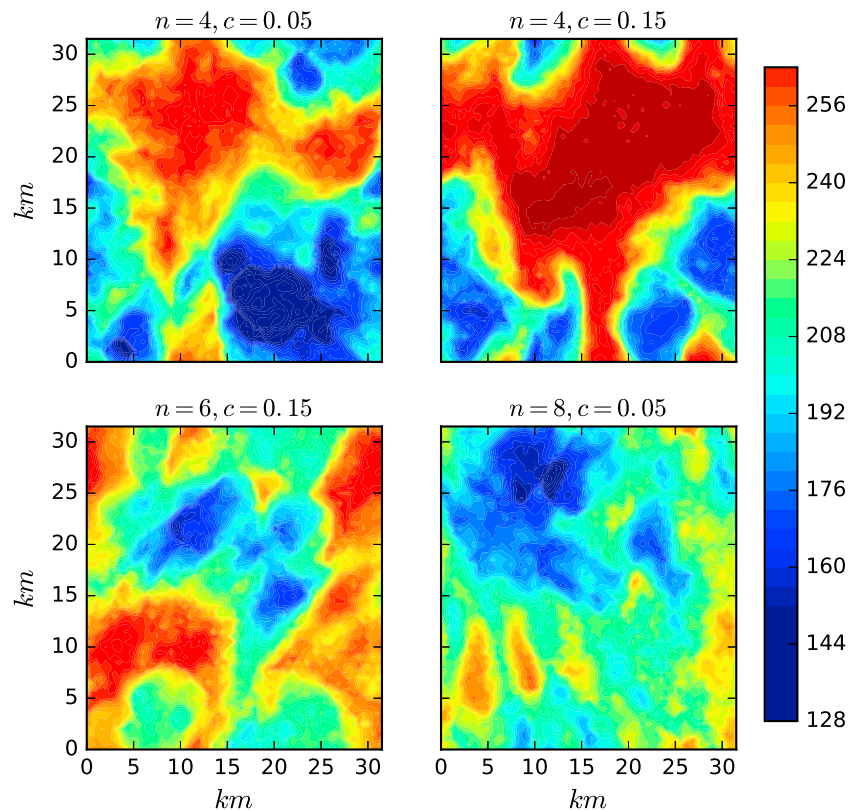


**Figure 7.** Snapshots of the outgoing longwave radiation (OLR) in  $W/m^2$ , as a proxy for convective organization.

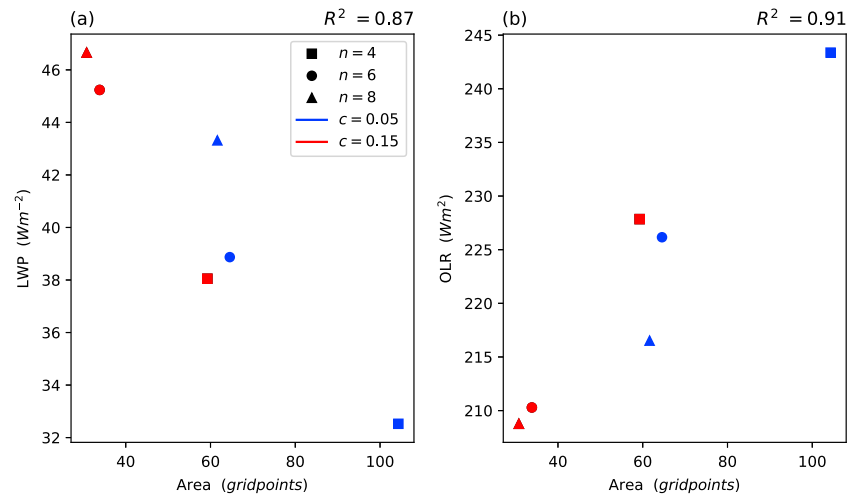


**Figure 8.** Relationship between the area of convective updraft in the domain and (a) mean liquid water path and (b) mean OLR.

precipitation. This is somewhat unexpected given the reduction in mean convective mass flux of updraft and mean relative humidity in stronger damping case. However, it agrees well with the strength of cold pools in Figure 5, as heavier precipitation usually tends to produce more intense cold pools.

### 3.3. Radiative Fluxes and Cloud Radiative Forcing

In this section, we focus on the effect of radiative fluxes and cloud radiative forcing resulting from changes in column water vapor and cloud fraction caused by divergence damping. Table 1 shows the reflected shortwave radiative flux at the top of the atmosphere (TOA), the downward shortwave flux reaching the surface, the OLR at TOA (OLR), and the downward longwave radiative flux at the surface.

In agreement with the amount of cloudiness induced by convective mass flux of updrafts, simulation with strongest damping ( $n = 4, c = 0.15$ ), in which cloud fraction is minimal, has the least reflected shortwave at TOA. Therefore, the surface receives more shortwave, which increases the amount of upward longwave leaving the atmosphere (OLR) and decreases the downward longwave at the surface.

On the other end, the simulation in which divergent damping is minimized in order and magnitude, ( $n = 8, c = 0.05$ ), with most cloudiness coverage and humidity, has most shortwave reflection at TOA, and least received shortwaves at the surface. Longwaves are maximum at the surface, and minimum at TOA (or OLR). Response of radiative fluxes remains monotonic with the order and magnitude of the damping, and the differences at a given divergence damping order for different coefficients become smaller as the order increases. Generally, the differences between different orders at a given coefficient are smaller.

Changes in radiative fluxes cause clouds to exhibit changes in their radiative forcing. Figure 10 shows cloud radiative forcing defined as clear-sky minus all-sky radiative fluxes at the top of atmosphere for longwave (LWCRF), shortwave (SWCRF) and their sum (NET CRF). Negative SWCRF (Figure 9a) and positive LWCRF (Figure 10b) increase monotonically as the damping order and magnitude decrease. Monotonicity in NET CRF (Figure 10c), however, is not clear. Weaker damping magnitude ( $c = 0.05$  in blue squares) is maxima for the sixth order and exceeds that of stronger damping magnitude ( $c = 0.15$  in red squares) except for the eighth order. Differences between weak and strong damping at a given divergence damping order become smaller in absolute value for the largest (eighth) order.

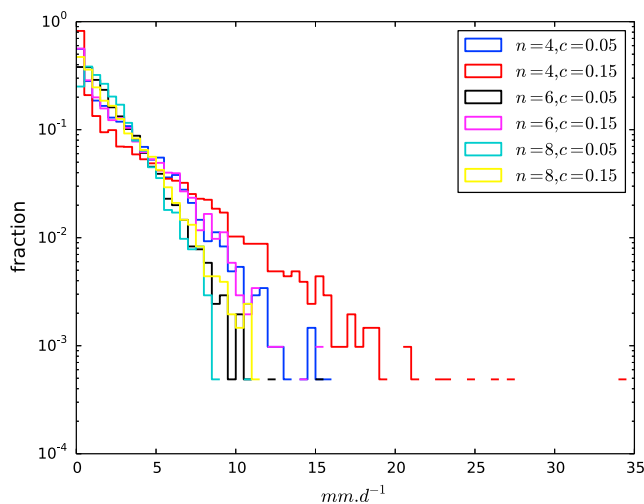


**Figure 9.** As in Figure 5 but for precipitation frequency distribution where precipitation is in 0.5 mm/day bins ranging from 0 to 35 mm/day, calculated from 6-hr averages for all grid points.

**Table 1**

*Radiative Fluxes: Upward Shortwave and Longwave at the Top of Atmosphere (SWTOA and OLR, Respectively) and Downward Shortwave and Longwave at the Surface (SWSFC and LWSFC, Respectively), for Different Divergence Damping Order ( $n$ ) and Coefficient ( $c$ )*

$n$	$c$	SWTOA	SWSFC	OLR	LWSFC
$n = 4$	$c = 0.05$	96.34	239.21	227.85	400.07
	$c = 0.15$	84.76	253.89	243.37	390.11
$n = 6$		<b>11.58</b>	<b>-14.69</b>	<b>-15.53</b>	<b>9.95</b>
	$c = 0.05$	109.49	225.36	210.29	405.38
	$c = 0.15$	98.19	237.44	226.16	400.27
$n = 8$		<b>11.30</b>	<b>-12.08</b>	<b>-15.86</b>	<b>5.11</b>
	$c = 0.05$	111.95	222.34	208.77	407.92
	$c = 0.15$	105.78	229.48	216.52	403.32
		<b>6.16</b>	<b>-7.14</b>	<b>-7.75</b>	<b>4.59</b>

Note. Numbers in bold are the difference between  $c = 0.05$  and  $c = 0.15$  at the same order. All magnitudes are in  $W/m^2$ .

#### 4. Discussion

Divergence damping is introduced in numerical models to prevent energy buildup and noise at the grid scale. This study demonstrates sensitivity of the RCE climate simulated by the FV3-based CRM operating at cloud-resolving resolution to dynamical damping of the divergent component of the horizontal flow, which changes the strength, width, and frequency of convective updrafts and hence the effective organization of convection. Such changes in organization lead to dramatic changes in free tropospheric humidity, cold pools, OLR, precipitation statistics, and cloud cover and cloud radiative effects. While our experiments here are conducted over a small domain aiming to discourage self-aggregation, in larger domains, convection in FV3 exhibits an aggregated state that does not appear to be sensitive to the subgrid diffusion. This raises some uncertainty about the mechanisms controlling the degree of convective organization discussed here.

Divergence damping in the model utilized here is the only explicit subgrid scheme applied to the horizontal wind field. In the vertical, the only diffusive component of the model is the explicit boundary layer. Other explicit subgrid schemes typically used in CRMs (that we do not use here) include Smagorinsky-type damping in the horizontal, horizontal hyper-diffusion, and both physical and numerical vertical diffusion. The coefficients for these subgrid schemes are also tunable, just as they are for divergence damping in FV3, and one would expect sensitivities of the RCE climate to this tuning. Although it is possible that some of the sensitivity to subgrid parameters described here is special to either the FV3 dynamical core or the AM4 physics, Zhou (2016, Ch. 5) and Tompkins and Semie (2017) suggest that similar sensitivity occurs in other models. It is not clear how these RCE simulations can be optimized in the subgrid parameter space with reference only to this RCE configuration for which there are no observations. One approach is to simulate RCE at much higher horizontal resolution, with the hope of generating something closer to a benchmark for this idealized configuration. An alternative and more common approach is to simulate particular observed convective events. Subgrid parameters are then optimized to produce a simulated state matching that observed (e.g., Grabowski et al., 1998; Khairoutdinov et al., 2009; Xu & Randall, 1996). The same settings would then be used for RCE simulations. The sensitivity documented here emphasizes the importance of these validation strategies.

Realistic configurations of numerical models invariably damp grid-scale motions, either explicitly or implicitly. Therefore, we do not agree that the conclusions of the inviscid low-order analysis of Skamarock (2008) concerning the accuracy of grid-scale modes are relevant to these or to any other realistic simulations from an FV3-based model. We hope that emerging full-physics model intercomparisons, such as the Radiative-Convective Equilibrium Model Intercomparison Project (RCMIP; Wing et al., 2018), will prove to be a more useful way of evaluating model characteristics under conditions more appropriate for real-world applications.

Another question these results raise is about the progression toward global cloud-resolving modeling. As global model approach the gray zone, say  $dx \sim 1\text{--}10$  km (Jeevanjee, 2017), at what point should modelers begin to worry about the effects of numerical subgrid formulations on convection that we find here? And how should they balance this concern with a continued need to dissipate energy and noise at small scales? It will also be important to determine the extent to which this sensitivity in the idealized RCE configuration translates into sensitivity in more realistic horizontally inhomogeneous configurations. This question is, in turn, closely

related to the question of how to balance the need to dissipate energy and noise at small scales with the need to resolve the convective processes that we find here? And how should they balance this concern with a continued need to dissipate energy and noise at small scales? It will also be important to determine the extent to which this sensitivity in the idealized RCE configuration translates into sensitivity in more realistic horizontally inhomogeneous configurations. This question is, in turn, closely

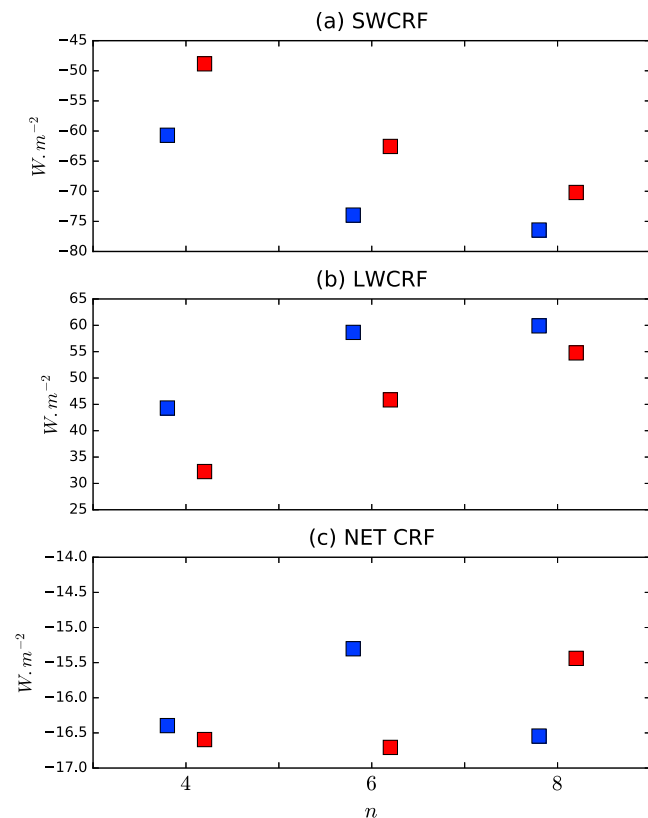


**Figure 10.** Cloud radiative forcing defined as clear-sky minus all sky radiative fluxes of (a) shortwaves, (b) longwaves, and (c) and sum of shortwaves and longwaves at the top of the atmosphere in  $W/m^2$ . The blue and red squares are for coefficient  $c = 0.05$  and  $c = 0.15$  for a given damping order  $n$ , respectively.

connected to the broader question of the extent to which the convective organization seen in many RCE simulations is relevant to convective organization in nature and more realistic model configurations.

### Acknowledgments

This work was prepared by U. A. under award NA14OAR4320106 from the National Oceanic and Atmospheric Administration, U.S. Department of Commerce. The statements, findings, conclusions, and recommendations are those of the authors and do not necessarily reflect the views of the National Oceanic and Atmospheric Administration, or the U.S. Department of Commerce. The authors would like to thank Leo Donner, Shian-Jiann Lin, Ming Zhao, and Xi Chen for helpful comments and suggestions. U. A. would like to thank Linjiong Zhuo for numerous insightful discussions. The model and the output data were made available and can be accessed via websites <https://github.com/NOAA-GFDL/AM4> and <https://github.com/uanber/GFDL-FV3/>, respectively.

### References

- Bretherton, C. S., Blossey, P. N., & Khairoutdinov, M. (2005). An energy-balance analysis of deep convective self-aggregation above uniform SST. *Journal of the Atmospheric Sciences*, *62*(12), 4273–4292. <https://doi.org/10.1175/JAS3614.1>
- Donner, L. J., Wyman, B. L., Hemler, R. S., Horowitz, L. W., Ming, Y., Zhao, M., et al. (2011). The dynamical core, physical parameterizations, and basic simulation characteristics of the atmospheric component AM3 of the GFDL Global Coupled Model CM3. *Journal of Climate*, *24*(13), 3484–3519. <https://doi.org/10.1175/2011JCLI3955.1>
- Durran, D. R. (1999). *Numerical methods for wave equations in geophysical fluid dynamics* (1st ed., p. 465). New York: Springer.
- Feng, Z., Hagos, S., Rowe, A. K., Burleyson, C. D., Martini, M. N., & de Szoeke, S. P. (2015). Mechanisms of convective cloud organization by cold pools over tropical warm ocean during the AMIE/DYNAMO field campaign. *Journal of Advances in Modeling Earth Systems*, *7*(2), 357–381. <https://doi.org/10.1002/2014MS000384>
- Grabowski, W. W., Wu, X., Moncrieff, M. W., & Hall, W. D. (1998). Cloud-resolving modeling of cloud systems during Phase III of GATE. Part II: Effects of resolution and the third spatial dimension. *Journal of the Atmospheric Sciences*, *55*(21), 3264–3282. [https://doi.org/10.1175/1520-0469\(1998\)055<3264:CRMOC>2.0.CO;2](https://doi.org/10.1175/1520-0469(1998)055<3264:CRMOC>2.0.CO;2)
- Held, I. R., Hemler, R. S., & Ramaswamy, V. (1993). Radiative-convective equilibrium with explicit two-dimensional moist convection. *Journal of the Atmospheric Sciences*, *50*(23), 3909–3927. [https://doi.org/10.1175/1520-0469\(1993\)050<3909:RCEWET>2.0.CO;2](https://doi.org/10.1175/1520-0469(1993)050<3909:RCEWET>2.0.CO;2)
- Holloway, C. E., Woolnough, S. J., & Lister, G. M. S. (2013). The effects of explicit versus parameterized convection on the MJO in a large-domain high resolution tropical case study. Part 1: Characterisation of large scale organisation and propagation. *Journal of the Atmospheric Sciences*, *70*(5), 1342–1369. <https://doi.org/10.1175/JAS-D-12-0227.1>
- Jablonowski, C., & Williamson, D. L. (2011). The pros and cons of diffusion, filters and fixers in atmospheric general circulation models. In P. H. Lauritzen, C. Jablonowski, M. A. Taylor, & R. D. Nair (Eds.), *Numerical Techniques for Global Atmospheric Models, Lecture Notes in Computational Science and Engineering*, (Vol. 80, pp. 381–493). Berlin: Springer.
- Jeevanjee, N. (2017). Vertical velocity in the gray zone. *Journal of Advances in Modeling Earth Systems*, *9*, 2304–2316. <https://doi.org/10.1002/2017MS001059>
- Jeevanjee, N., & Romps, D. M. (2015). Effective buoyancy, inertial pressure, and the mechanical generation of boundary layer mass flux by cold pools. *Journal of the Atmospheric Sciences*, *72*(8), 3199–3213. <https://doi.org/10.1175/JAS-D-14-0349.1>
- Khairoutdinov, M. F., Krueger, S. K., Moeng, C.-H., Bogenschutz, P. A., & Randall, D. (2009). Large-eddy simulation of maritime deep tropical convection. *Journal of Advances in Modeling Earth Systems*, *1*, 15. <https://doi.org/10.3894/JAMES.2009.1.15>
- Klein, S. A., Pincus, R., Hannay, C., & Xu, K.-M. (2005). How might a statistical cloud scheme be coupled to a mass-flux convection scheme? *Journal of Geophysical Research*, *110*, D15S06. <https://doi.org/10.1029/2004JD005017>
- Kuang, Z., & Hartmann, D. (2007). Testing the fixed anvil temperature hypothesis in a cloud-resolving model. *Journal of Climate*, *20*(10), 2051–2057. <https://doi.org/10.1175/JCLI4124.1>
- Lin, S.-J. (2004). A “vertically Lagrangian” finite-volume dynamical core for global models. *Monthly Weather Review*, *132*(10), 2293–2307. [https://doi.org/10.1175/1520-0493\(2004\)132<2293:AVLFDC>2.0.CO;2](https://doi.org/10.1175/1520-0493(2004)132<2293:AVLFDC>2.0.CO;2)
- Lin, S.-J., & Harris, L. M. (2016). Explicit diffusion in GFDL FV3. Technical document available at: [https://www.gfdl.noaa.gov/wp-content/uploads/2017/09/Diffusion\\_operators.pdf](https://www.gfdl.noaa.gov/wp-content/uploads/2017/09/Diffusion_operators.pdf)
- Mellor, G. L., & Yamada, T. (1982). Development of a turbulence closure model for geophysical fluid problems. *Reviews of Geophysics and Space Physics*, *20*, 851–875.
- Muller, C. J., & Held, I. (2012). Detailed investigation of the self-aggregation of convection in cloud-resolving simulations. *Journal of the Atmospheric Sciences*, *69*(8), 2551–2565. <https://doi.org/10.1175/JAS-D-11-0257.1>
- Nakanishi, M., & Niino, H. (2006). An improved Mellor–Yamada level-3 model: Its numerical stability and application to a regional prediction of advection fog. *Boundary-Layer Meteorology*, *119*, 397–407. <https://doi.org/10.1007/s10546-005-9030-8>
- Putman, W. M., & Lin, S.-J. (2007). Finite-volume transport on various cubed-sphere grid. *Journal of Computational Physics*, *227*, 55–78.
- Robe, F. R., & Emanuel, K. A. (2001). The effect of vertical wind shear on radiative-convective equilibrium states. *Journal of the Atmospheric Sciences*, *58*(11), 1427–1445. [https://doi.org/10.1175/1520-0469\(2001\)058<1427:TEOVWS>2.0.CO;2](https://doi.org/10.1175/1520-0469(2001)058<1427:TEOVWS>2.0.CO;2)
- Romps, D. M. (2011). Response of tropical precipitation to global warming. *Journal of the Atmospheric Sciences*, *68*(1), 123–138. <https://doi.org/10.1175/2010JAS3542.1>
- Romps, D. M. (2014). An analytical model for tropical relative humidity. *Journal of Climate*, *27*(19), 7432–7449. <https://doi.org/10.1175/JCLI-D-14-00255.1>
- Rotunno, R., Klemp, J. B., & Weisman, M. L. (1988). A theory for strong, long-lived squall lines. *Journal of the Atmospheric Sciences*, *45*(3), 463–485. [https://doi.org/10.1175/1520-0469\(1988\)045<0463:atfsl>2.0.CO;2](https://doi.org/10.1175/1520-0469(1988)045<0463:atfsl>2.0.CO;2)
- Skamarock, W. C. (2008). A linear analysis of the NCAR CCSM finite-volume dynamical core. *Monthly Weather Review*, *136*(6), 2112–2119. <https://doi.org/10.1175/2007MWR2217.1>
- Tao, W.-K., Simpson, J., Shie, C.-L., Zhou, B., Lau, K. M., & Moncrieff, M. (1999). Equilibrium states simulated by cloud resolving models. *Journal of the Atmospheric Sciences*, *56*(17), 3128–3139. [https://doi.org/10.1175/1520-0469\(1999\)056<3128:ESSBCR>2.0.CO;2](https://doi.org/10.1175/1520-0469(1999)056<3128:ESSBCR>2.0.CO;2)
- Taylor, M. A., & Fournier, A. (2010). A compatible and conservative spectral element method on unstructured grids. *Journal of Computational Physics*, *229*(17), 5879–5895. <https://doi.org/10.1016/j.jcp.2010.04.008>
- Tompkins, A. M. (2001). Organization of tropical convection in low vertical wind shears: The role of cold pools. *Journal of the Atmospheric Sciences*, *58*(13), 1650–1672. [https://doi.org/10.1175/1520-0469\(2001\)058<1650:OOTCIL>2.0.CO;2](https://doi.org/10.1175/1520-0469(2001)058<1650:OOTCIL>2.0.CO;2)
- Tompkins, A. M. (2002). A prognostic parameterization for the subgrid scale variability of water vapor and clouds in large-scale models and its use to diagnose cloud cover. *Journal of the Atmospheric Sciences*, *59*(12), 1917–1942. [https://doi.org/10.1175/1520-0469\(2002\)059<1917:APPFTS>2.0.CO;2](https://doi.org/10.1175/1520-0469(2002)059<1917:APPFTS>2.0.CO;2)
- Tompkins, A. M., & Craig, G. C. (1999). Sensitivity of tropical convection to sea surface temperature in the absence of large-scale flow. *Journal of Climate*, *12*(2), 462–476. [https://doi.org/10.1175/1520-0442\(1999\)012<0462:SOTCTS>2.0.CO;2](https://doi.org/10.1175/1520-0442(1999)012<0462:SOTCTS>2.0.CO;2)
- Tompkins, A. M., & Semie, A. G. (2017). Organization of tropical convection in low vertical wind shears: Role of updraft entrainment. *Journal of Advances in Modeling Earth Systems*, *9*(2), 1046–1068. <https://doi.org/10.1002/2016MS000802>
- Torri, G., Kuang, Z., & Tian, Y. (2015). Mechanisms for convection triggering by cold pools. *Geophysical Research Letters*, *42*, 1943–1950. <https://doi.org/10.1002/2015GL063227>

- Williamson, D. L. (2008a). Convergence of aqua-planet simulations with increasing resolution in the Community Atmospheric Model, Version3. *Tellus*, *60A*, 848–862.
- Williamson, D. L. (2008b). Equivalent finite volume and Eulerian spectral transform horizontal resolutions established from aqua-planet simulations. *Tellus*, *60A*, 839–847.
- Wing, A. A., Reed, K. A., Satoh, M., Stevens, B., Bony, S., & Ohno, T. (2018). Radiative-Convective Equilibrium Model Intercomparison Project. *Geoscientific Model Development*, *11*(2), 793–813. <https://doi.org/10.5194/gmd-11-793-2018>
- Xu, K. M., & Randall, D. A. (1996). A semiempirical cloudiness parameterization for use in climate models. *Journal of the Atmospheric Sciences*, *53*(21), 3084–3102. [https://doi.org/10.1175/1520-0469\(1996\)053<3084:ASCPFU>2.0.CO;2](https://doi.org/10.1175/1520-0469(1996)053<3084:ASCPFU>2.0.CO;2)
- Zhao, M., Golaz, J.-C., Held, I. M., Guo, H., Balaji, V., Benson, R., et al. (2018a). The GFDL global atmosphere and land model AM4.0/LM4.0: 1. Simulation characteristics with prescribed SSTs. *Journal of Advances in Modeling Earth Systems*, *10*, 691–734. <https://doi.org/10.1002/2017MS001208>
- Zhao, M., Golaz, J.-C., Held, I. M., Guo, H., Balaji, V., Benson, R., et al. (2018b). The GFDL global atmosphere and land model AM4.0/LM4.0: 2. Model description, sensitivity studies, and tuning strategies. *Journal of Advances in Modeling Earth Systems*, *10*, 735–769. <https://doi.org/10.1002/2017MS001209>
- Zhao, M., Held, I. M., & Lin, S.-J. (2012). Some counterintuitive dependencies of tropical cyclone frequency on parameters in a GCM. *Journal of the Atmospheric Sciences*, *69*(7), 2272–2283. <https://doi.org/10.1175/JAS-D-11-0238.1>
- Zhou, W. (2016). *Non-rotating and rotating radiative-convective equilibria*. Princeton, NJ: Princeton University. Retrieved from <http://arks.princeton.edu/ark:/88435/dsp01n009w468h>